WASP-80b has a dayside within the T-dwarf range[*]

Amaury H. M. J. Triaud,[1,2,3][†] Michaël Gillon,[4] David Ehrenreich,[5] Enrique Herrero,[6]
Monika Lendl,[4,5] David R. Anderson,[7] Andrew Collier Cameron,[8] Laetitia Delrez,[4]
Brice-Olivier Demory,[9] Coel Hellier,[7] Kevin Heng,[10] Emmanuel Jehin,[4]
Pierre F. L. Maxted,[7] Don Pollacco,[11] Didier Queloz,[9] Ignasi Ribas,[6] Barry Smalley,[7]
Alexis M. S. Smith[12] and Stéphane Udry[5]

Affiliations are listed at the end of the paper

ABSTRACT

WASP-80b is a missing link in the study of exoatmospheres. It falls between the warm
Neptunes and the hot Jupiters and is amenable for characterization, thanks to its host star's
properties. We observed the planet through transit and during occultation with *Warm Spitzer*.
Combining our mid-infrared transits with optical time series, we find that the planet presents
a transmission spectrum indistinguishable from a horizontal line. In emission, WASP-80b
is the intrinsically faintest planet whose dayside flux has been detected in both the 3.6 and
4.5 μm *Spitzer* channels. The depths of the occultations reveal that WASP-80b is as bright and
as red as a T4 dwarf, but that its temperature is cooler. If planets go through the equivalent
of an L–T transition, our results would imply that this happens at cooler temperatures than
for brown dwarfs. Placing WASP-80b's dayside into a colour–magnitude diagram, it falls
exactly at the junction between a blackbody model and the T-dwarf sequence; we cannot
discern which of those two interpretations is the more likely. WASP-80b's flux density is as
low as GJ 436b at 3.6 μm; the planet's dayside is also fainter, but bluer than HD 189733Ab's
nightside (in the [3.6] and [4.5]*Spitzer* bands). Flux measurements on other planets with
similar equilibrium temperatures are required to establish whether irradiated gas giants, such
as brown dwarfs, transition between two spectral classes. An eventual detection of methane
absorption in transmission would also help lift that degeneracy. We obtained a second series of
high-resolution spectra during transit, using HARPS. We reanalyse the Rossiter–McLaughlin
effect. The data now favour an aligned orbital solution and a stellar rotation nearly three times
slower than stellar line broadening implies. A contribution to stellar line broadening, maybe
macroturbulence, is likely to have been underestimated for cool stars, whose rotations have
therefore been systematically overestimated.

Key words: planets and satellites: atmospheres – planets and satellites: individual:
WASP-80b – binaries: eclipsing – brown dwarfs – Hertzsprung–Russell and colour–magnitude
diagrams – stars: late-type.

1 INTRODUCTION

Orbital migration, disc driven or dynamical in origin, has created hot
Jupiters (Mayor & Queloz 1995; Lin, Bodenheimer & Richardson

1996; Rasio & Ford 1996). Having a high probability to transit,
they opened up the opportunity to study the atmospheric content
of extrasolar gas giants without having to spatially resolve them
(e.g. Seager & Deming 2010). In addition, there is hope that the
chemical abundances of these planets carries information about
where they formed (Öberg, Murray-Clay & Bergin 2011). This
can be combined with those systems' architectures (multiplicity,
eccentricity, orbital inclination) and give a greater appreciation of
the processes generating the diversity and width of parameter space
that exoplanets occupy.

Their proximity to their host star influences what we can know
about these gas giants. For instance, water in the upper atmosphere

of the planet will be in the gas phase as a result of the intense irradiation from the host star; its abundance can be measured. This enables us to infer the oxygen content, a quantity which is hard to obtain in the case of a cold planet such as Jupiter (Madhusudhan et al. 2014). Then, the carbon to oxygen abundance ratio can be quantified and linked to the chemistry of the protoplanetary disc and ultimately, to the formation process of the planet (Bolton & the Juno Science Team 2010).

Proximity also fosters the appearance of a host of exotic phenomena which remain to be fully investigated. For instance, irradiation causes hot Jupiters to be inflated, whose exact cause (or causes) continues to be an active area of research (e.g. Demory & Seager 2011 and references there-in). The temperatures of the majority of hot Jupiters whose atmospheres have been studied, are in the range 1500–2000 K. Their densities are lower than colder planets which makes them practical targets for transmission spectroscopy, at transit. Their bloated size and elevated temperature are also advantages when carrying emission spectroscopy, at occultation.

Hot Jupiters have sizes and dayside temperatures that makes them resemble late M-dwarfs and L-type brown dwarfs. They share a common colour–magnitude space (Triaud 2014). These non-irradiated, self-luminous objects are covered by dust clouds, produced by the condensation of various species such as silicates, aluminium and iron bearing molecules as well as titanium and vanadium oxides (Kirkpatrick 2005), which become patchy with decreasing temperatures (Ackerman & Marley 2001; Burgasser et al. 2002; Artigau et al. 2009; Radigan et al. 2012; Gillon et al. 2013; Buenzli et al. 2014; Crossfield et al. 2014). In the near-infrared bands Y, J, H and K, the L–T transition is characterized by a blueward shift where the hotter, deeper parts of the atmosphere start becoming visible through cloud clearings. In the mid-IR [3.6] and [4.5 µm] bands, that transition is defined by a redward slope, produced in part by a shift of the blackbody peak towards cooler temperatures but also, by an increase in CH_4 absorption (and its associated reduction in CO and CO_2) (Kirkpatrick 2005).

The presence of clouds and hazes is suspected to hamper the detection of molecules in the transmission spectra of hot Jupiters (e.g. Sing et al. 2011; Jordán et al. 2013; Mandell et al. 2013; Pont et al. 2013). If the analogy between self-luminous ultracool dwarfs and irradiated gas giants holds, then planets with daysides similar to mid- to late-T dwarfs ought to be mostly cloud free, presenting to our line of sight a clear terminator with strong methane absorption. In the two *Spitzer* bands we used, a T-dwarf-like planet would have an illuminated face redder than the typical hot Jupiter when using the two *Warm Spitzer* channels (Triaud et al. 2014).

WASP-80b is a special planet. This gas giant, discovered by the WASP Collaboration (Pollacco et al. 2006; Collier Cameron et al. 2007; Hellier et al. 2012), orbits a bright ($V = 11.9$, $K = 8.4$, $W1 = 8.28$, $W2 = 8.31$) late K dwarf/early M-dwarf. Despite a 3 d orbit, typical of hot Jupiters, it has an equilibrium temperature close to only 800 K (Triaud et al. 2013). This is one of the coolest gas giants whose atmosphere can be studied in transmission and emission using current instrumentation. As such, it is an obvious target to observe to verify how temperature affects planetary spectra and to continue the exploration in colour–magnitude space. This is one of only a few systems expected to resemble a T-dwarf (Triaud et al. 2014). In addition, of the other planets with similar or colder temperatures that have been studied, all are Neptune-like planets, orbiting M-dwarfs. WASP-80b fills an empty space between those small, warm Neptunes, and the more massive and large, hot Jupiters. The warm Neptunes mostly have featureless transmission spectra (Ehrenreich et al. 2014; Knutson et al. 2014; Kreidberg et al.

2014), with the notable exception of HAT-P-11b (Fraine et al. 2014). WASP-80b has a larger scaleheight, more amenable for transmission spectroscopy.

To improve the characterization of this fascinating planet, we observed some of its transits and occultations at 3.6 and 4.5 µm with *Spitzer*, and gathered new ground-based transit photometry and spectroscopy. We combine these new observations with published high-quality data, and perform a global analysis of the resulting extensive data set. We present here the results of this work. Our paper is simply organized: we first present our data collection and analysis, and then discuss our results and conclude.

2 DATA COLLECTION AND ANALYSIS

We used the photometric and spectroscopic data presented in Triaud et al. (2013) as well as the light curves collected and analysed by Mancini et al. (2014); see Table A1 and Fig. A3. To these, we add ground- and space-based photometry, described in the first subsection, and new spectroscopic information reported in the second subsection.

2.1 Broad-band photometry at transit and at occultation

2.1.1 *New Sloan-z′ and Gunn-r′ transit photometry with TRAPPIST and* Euler

We captured three additional transits during the 2013 season, using TRAPPIST (Jehin et al. 2011). One of these – on the night starting on 2013-06-15 – was acquired in tandem with the *Euler* telescope. They are also simultaneous with the DFOSC and GROND light curves presented by Mancini et al. (2014), and with the Rossiter–McLaughlin effect described in the following subsection. That night, five telescopes observed WASP-80b simultaneously from La Silla.

The TRAPPIST observations made use of a Sloan $z′$ filter, with each frame exposed for 13 s. The transit observed with *Euler* was acquired through a Gunn-$r′$ filter, and an exposure time of 50 s. Observations were set up similarly on both telescopes. Notably, we kept the positions of each star on the CCD chip within a box of a few pixels. This is achieved using a 'software guiding' system which regularly derives an astrometric solution on the science images, and sends pointing corrections to the mount when needed. This improves the photometric precision by reducing the instrumental noise due to flat-fielding errors. Table A1 presents a log of the observations.

After a standard pre-reduction (bias, dark, flat-field correction), stellar fluxes were extracted from our images using the IRAF/DAOPHOT[1] aperture photometry software (Stetson 1987). For each transit, several sets of reduction parameters were tested. We kept the set yielding the most precise photometry on the stars having a brightness similar to WASP-80. After a careful selection of reference stars, differential photometry was then obtained. The resulting light curves are shown in the appendix (Fig. A3).

2.1.2 Spitzer *transit and occultation photometry at 3.6 and 4.5* µ*m*

We requested time to observe WASP-80 with *Spitzer* (PID 90159; Triaud) and captured six eclipses of the system with IRAC (Fazio

---

[1] IRAF is distributed by the National Optical Astronomy Observatory, which is operated by the Association of Universities for Research in Astronomy, Inc., under cooperative agreement with the National Science Foundation.

et al. [2004]). We obtained data covering one transit and two occultations at 3.6 μm and one transit and two occultations at 4.5 μm. The scheduling of these observations was based on the orbital solution presented by Triaud et al. ([2013]). We used the subarray mode (32 × 32 pixels, 1.2 arcsec pixel^{-1}) with exposure times of 0.4 s (3.6 μm) and 2 s (4.5 μm). The resulting sets of 64 individual subarray images were calibrated by the *Spitzer* pipeline version S19.1.0 and are available on the *Spitzer* Heritage Archive Database.[2]

The data were reduced in the same way for all six time series. We first converted fluxes from the *Spitzer* units of specific intensity (MJy sr^{-1}) to photon counts. We then performed aperture photometry on each subarray image with IRAF/DAOPHOT. We tested different aperture radii and background annuli, and found the best results with an aperture radius of 2.5 pixels and a background annulus extending from 11 to 15.5 pixels from the centre of the point spread function (PSF). We measured the centre and width of the PSF (FWHM) by fitting a 2D Gaussian profile on each image. We then inspected at the *x*–*y* distribution of the measurements, and discarded the few measurements having a visually discrepant position relative to the bulk of the data. For each block of 64 subarray images, we then discarded the discrepant values for the measurements of flux, background, *x* and *y* positions, and PSF widths in the *x*- and *y*-direction, using a 10σ median clipping for the six parameters. We averaged the remaining values, taking the errors on the average flux measurements as photometric errors. At this stage, we used a moving median filter in flux on the resulting light curves to discard outlier measurements due to cosmic hits, for example. The resulting light curves can be inspected in the appendix, in Figs A1 and A2.

2.2 HARPS observations at transit

On the night starting on 2013-06-15, simultaneously with much of the ground-based photometry, we obtained a series of 26 spectra with HARPS (Prog. ID 091.C-0184; Triaud) at a cadence of approximately 10 min. These new data are of higher quality than the transit spectroscopy presented in Triaud et al. ([2013]) as a result of better weather conditions (clear sky, 0.6 arcsec seeing) and higher cadence. Seven additional spectra were obtained on the nights leading to and following the transit night. They helped further contain the orbital parameters.

The data were reduced using the standard HARPS reduction software, and the radial velocities were extracted by cross-correlating each spectrum with a K5 mask, as was done in Triaud et al. ([2013]).

2.3 Global data analysis

Strong constraints on the system parameters can be derived by performing a global Bayesian analysis of the photometric and radial velocity time series. We constructed the posterior probability distributions functions of the global model parameters using an adaptive Markov Chain Monte Carlo (MCMC) code described in Gillon et al. ([2014], and references therein).

Transits and occultations were modelled with the algorithm written by Mandel & Agol ([2002]). Each light curve is multiplied by a baseline model, which accounts for other astrophysical and instrumental effects resulting in photometric variations. A quadratic limb-darkening law was assumed for the transits. For each light curve, a baseline model (see Table A1) was selected by way of minimizing the Bayesian Information Criterion (Schwarz [1978]). The radial velocities were modelled by a Keplerian orbit for the star

combined to a systemic velocity, and to the spectroscopic transit model of Giménez ([2006]).

For the ground-based light curves, a second-order time polynomial is systemically assumed for each baseline. It accounts for a possible low-frequency stellar variability, for a difference in colour between the target and its comparison stars, and for their consequent differential extinction. The modelling of other effects (dependence of fluxes on full width at half-maximum (FWHM), on position, meridian flip) were also required for a few light curves (see Table A1).

For the *Spitzer* photometry, our baseline models representing the well-documented 'ramp' and 'phase-pixel' effects (e.g. Knutson et al. [2008]; Lewis et al. [2013]), are similar to those employed in the analysis of GJ 1214 (Gillon et al. [2014]); we refer the reader to that paper for a detailed description.

The only informative prior probability distribution functions assumed in our analysis are for the stellar mass $M_\star$, effective temperature $T_{\rm eff}$, metallicity [Fe/H], and for the limb-darkening coefficients of each bandpass. We assumed normal prior distributions $N(0.58, 0.05^2)$ M$_\odot$, $N(4145, 100^2)$ K, and $(-0.14, 0.16)$ dex, for $M_\star$, $T_{\rm eff}$ and [Fe/H], respectively (Triaud et al. [2013]). Normal prior distributions are also assumed for the coefficients u_1 and u_2 of the quadratic limb-darkening law. The parameters of our Gaussians were interpolated from the tables of Claret & Bloemen ([2011]) for each of the bandpasses we observed in, and corresponding to a star with $T_{\rm eff} = 4145 \pm 100$ K, $\log g_\star = 4.689 \pm 0.013$ dex and [Fe/H] $= -0.14 \pm 0.16$ dex (Triaud et al. [2013]). No priors were applied to the Rossiter–McLaughlin effect.[3]

A first chain of 10 000 steps was launched. It brought to our attention the need to rescale our photometric errors in order to account for an extra-white noise and for some correlated noise. We also estimated the amount of stellar noise ('jitter') in the radial velocities and added this quadratically to the radial velocity errors (see Gillon et al. [2012] for details). The error rescaling factors for the light curves are given in Table A1. For the CORALIE radial velocities, the deduced jitter noise was 8.1 m s^{-1}; the HARPS data required none. With errors corrected, we performed our main analysis that consisted of two chains composed of 100 000 steps. They converged according to the statistical test of Gelman & Rubin ([1992]). Table 1 collects our derived parameters and their 1σ confidence region.

The resulting light curves, corrected from systematic effects and co-added according to wavelength, are displayed in Fig. 1. The transits (Fig. 1a) have been binned in 2.5 min bins (for visual convenience only), and the occultations (Fig. 1b) in 5 min bins.

2.4 A study of the Rossiter–McLaughlin effect

In the discovery paper, we were unable to distinguish the impact parameter from zero, which led the fitting procedure of the Rossiter–McLaughlin effect to produce degenerate solutions for the projected spin–orbit angle β (e.g. Albrecht et al. [2011]; Triaud et al. [2011]). Here we study several possibilities, getting further into some details of the Rossiter–McLaughlin effect that the global analysis did not touch.

The Rossiter–McLaughlin effect was modelled using the prescription of Giménez ([2006]), in the same manner as in López-Morales et al. ([2014]), using priors as input for all the parameters except those controlling the effect. Both time series were adjusted

---

[3] The Rossiter–McLaughlin effect was analysed more in detail separately from the global analysis. The description is provided in Section 2.4.

Table 1. Results of our MCMC fits to the photometric and spectroscopic data for WASP-80. Errors on the last two digits of each parameters, are given in brackets. Asterisks mark parameters which are controlled by priors.

Parameters	Units	Values	
The star			
T_{eff}	K	$4143^{(+92)}_{(-94)}$	*
[Fe/H]	dex	$-0.13^{(+15)}_{(-17)}$	*
$\log g_\star$	cgs	$4.663^{(+15)}_{(-16)}$	
$M_\star$	$M_\odot$	$0.577^{(+51)}_{(-54)}$	*
$R_\star$	$R_\odot$	$0.586^{(+17)}_{(-18)}$	
$\rho_\star$	$\rho_\odot$	$2.875^{(+55)}_{(-86)}$	
$v\sin i_\star$	km s^{-1}	$1.27^{(+14)}_{(-17)}$	
The planet			
P	d	$3.067\,852\,34^{(+83)}_{(-79)}$	
T_0	BJD	$6487.425\,006^{(+23)}_{(-25)}$	
D (3.6 μm)	–	$0.029\,37^{(+13)}_{(-13)}$	
W	d	$0.088\,78^{(+13)}_{(-14)}$	
b	$R_\odot$	$0.215^{(+20)}_{(-22)}$	
K	m s^{-1}	$109.0^{(+3.1)}_{(-4.4)}$	
$\log g_p$	cgs	$3.145^{(+15)}_{(-16)}$	
$a/R_\star$	–	$12.63^{(+08)}_{(-13)}$	
M_p	M_{Jup}	$0.538^{(+35)}_{(-36)}$	
R_p (3.6 μm)	R_{Jup}	$0.999^{(+30)}_{(-31)}$	
ρ_p	ρ_{Jup}	$0.539^{(+29)}_{(-24)}$	
T_{eq}	K	$825^{(+19)}_{(-19)}$	
a	au	$0.0344^{(+10)}_{(-11)}$	
i_p	deg	$89.02^{(+11)}_{(-10)}$	
β	deg	$14^{(+15)}_{(-14)}$	
e	–	$0.002^{(+10)}_{(-02)}$	
ω	deg	$94^{(+120)}_{(-21)}$	
Star-to-planet ratio, $R_p/R_\star$			
0.47 μm	–	$0.170\,06^{(+77)}_{(-78)}$	
0.62 μm	–	$0.171\,69^{(+63)}_{(-62)}$	
0.77 μm	–	$0.172\,20^{(+64)}_{(-67)}$	
0.80 μm	–	$0.171\,73^{(+56)}_{(-56)}$	
0.90 μm	–	$0.171\,27^{(+69)}_{(-69)}$	
3.6 μm	–	$0.171\,37^{(+37)}_{(-39)}$	
4.5 μm	–	$0.172\,30^{(+40)}_{(-39)}$	
Occultation depths			
3.6 μm	ppm	$455^{(+100)}_{(-100)}$	
4.5 μm	ppm	$944^{(+64)}_{(-65)}$	
Brightness temperatures			
3.6 μm	K	$901^{(+68)}_{(-72)}$	
4.5 μm	K	$888^{(+58)}_{(-57)}$	

as a single data set, since no offset was detected between them. As in Triaud et al. (2013), we investigated three different propositions:

(i) using no priors on the projected stellar rotation $v\sin i_\star$;

(ii) using a prior, obtained from spectral line broadening, $v\sin i_\star = 3.55 \pm 0.33\,\mathrm{km\,s^{-1}}$ (Triaud et al. 2013);

(iii) applying a prior on $\beta = 0° \pm 10°$.

The first and third propositions produced similar, aligned, solutions, whereas the second converged on a inclined orbit. Thanks notably to the *Spitzer* photometry, which estimated a non-zero-impact parameter, β could be resolved ($54° \pm 7°$). However, this solution yields a poorer fit ($\Delta\chi^2 = 30.7$, for the same number of degrees of freedom) in part because it remains in 2σ tension with the adopted prior, supporting incompatibility between the value measured thanks to the Rossiter–McLaughlin effect and that estimated from stellar line broadening. We thus favour the results from the first proposition ($\beta = 14° \pm 14°$, $v\sin i_\star = 1.27 \pm 0.14\,\mathrm{km\,s^{-1}}$) and adopt them; they can be found in Table 1. Our estimation of $v\sin i_\star$ is thus an independent measurement.

The most likely fit and the data are displayed in Fig. 2.

3 DISCUSSION

3.1 About the Rossiter–McLaughlin effect

Thanks to the quality of our photometric data at transit and the much reduced influence of limb darkening in the mid-infrared, it was possible to precisely measure the impact parameter of WASP-80b. This lifts the degeneracy between $v\sin i_\star$ and β noted in Triaud et al. (2013), and enables us to show that the planet is on a coplanar orbit instead of inclined, as we had previously reported. The amplitude of the Rossiter–McLaughlin effect implies a slower rotation for the star than is estimated from stellar line broadening. The values are incompatible at the 7σ level. In Triaud et al. (2013), we took this difference as a sign that the planet's orbital plane was severely inclined (which the poor precision on the impact parameter then allowed), the data are now of sufficient quality to instead favour a coplanar solution. This brings this system more in line with the patterns of spin–orbit alignment with stellar host parameters proposed by Schlaufman (2010) and Winn et al. (2010).

We attempted to understand this discrepancy by verifying how $v\sin i_\star$ from spectral line broadening is affected by activity, and what the resulting Rossiter–McLaughlin effect would look like. To do this, we used tools developed in Herrero, Ribas & Jordi (2014).

The star is chromospherically active (Triaud et al. 2013; Mancini et al. 2014), and we could also detect, from the CORALIE spectra, that the Hα equivalent width of WASP-80 has a wider variation epoch to epoch than intranight measurements show, but presents no periodicity. Despite these indications of stellar activity, there is no rotational modulation in the photometry (Triaud et al. 2013). Some spot configurations can lead to weak photometric signal: (1) well centred and stable polar spots, (2) a continuously spotted active latitude or (3) a near homogeneously spotted surface. Those configurations were simulated, and produced slight differences in the estimation of $v\sin i_\star$, but the differences are less than 100 m s^{-1}. Fig. 3 shows a simulated Rossiter–McLaughlin effect for a spotless star, and one with large polar spots. The difference between both models is of the order of 1 m s^{-1} – well within error bars.

Furthermore, stellar spots outside of the transit chord produce a slope in the transmission spectrum (Jordán et al. 2013; McCullough et al. 2014). The important coverage necessary to significantly alter the Rossiter–McLaughlin effect would presumably leave a trace that is not detected in the multiwavelength photometry presented in Fig. 5.

Resolving this $v\sin i_\star$ discrepancy is outside of the range of topics this paper aimed to study; however, we note that most laws attempting to replicate macroturbulence in stars suggest that this
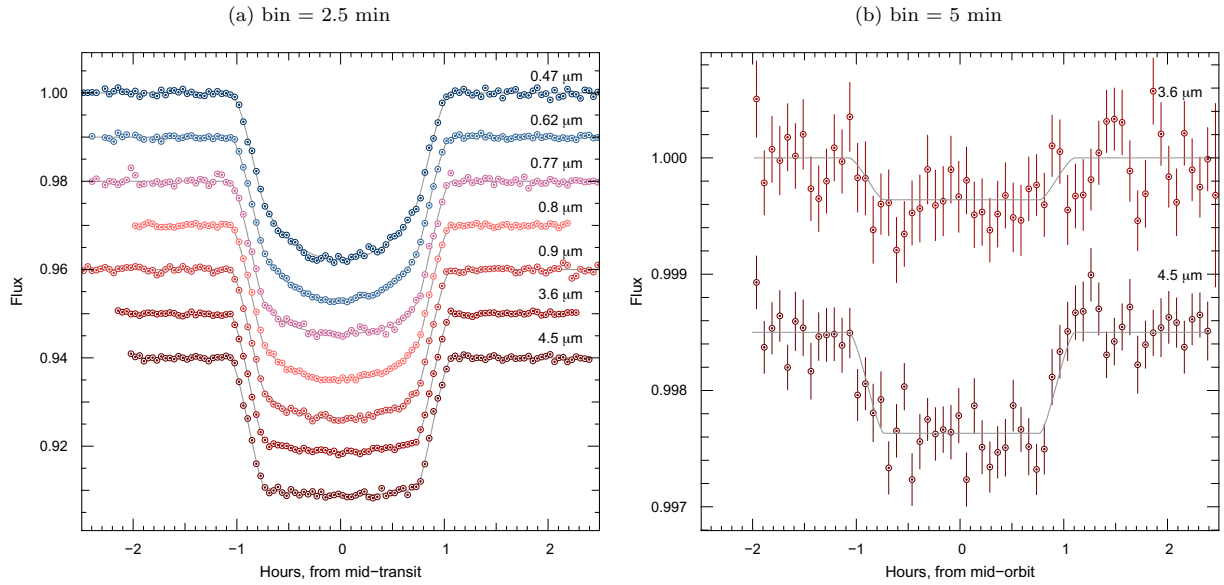
(a) bin = 2.5 min

(b) bin = 5 min

Figure 1. Photometric time series covering the transit (left-hand panel) and occultation (right-hand panel) of WASP-80. For visual convenience, the data are presented binned and vertically offset. They are labelled by central wavelength of the broad-band filter used. Uncorrected and unbinned data are available in the appendices.
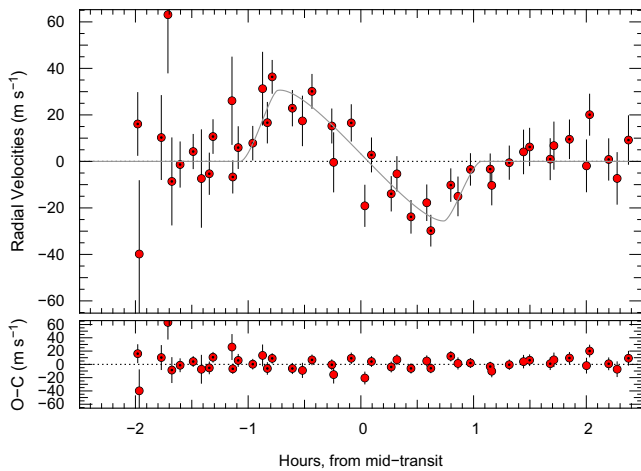

Figure 2. The Rossiter–McLaughlin effect caused by WASP-80b, as observed by HARPS, its most likely model and its corresponding residuals. The radial velocities are corrected for the Doppler reflex motion. Additional dark dots in the centre of some data points indicate the new data.

Figure 3. Simulation of the Rossiter–McLaughlin effect on a star similar to WASP-80. Two configurations are tested here. One where the star has no spots, and one where it possesses spots at the poles covering the upper and lower 40 degrees in latitude. This increases slightly the amplitude of the effect, because the fractional contribution to the stellar rotation hidden by the planet has gained in importance.

phenomenon's contribution to stellar line broadening decreases with stellar effective temperature, and vanishes for the coolest stars (e.g. Gray 2008). Doyle et al. (2014) have instead shown that it may plateau to a set value. Sadly, WASP-80 is too cool and falls out of their revised calibration. Our issues only highlights how tricky it is to estimate $v \sin i_\star$ from stellar line broadening. It reminds us of the vigilance we need to keep when including these values as priors in an analysis of the Rossiter–McLaughlin effect. Still, the fact remains that WASP-80 has wide lines compared to others stars with a similar $B - V$ (Triaud et al. 2013). If its width is equivalent to $v \sin i_\star = 1.3 \, \text{km s}^{-1}$ then all other late K and early M-dwarfs must be rotating much slower than they have been thought to do until now. As such, the Rossiter–McLaughlin effect may become a means to study the effect of macroturbulence by providing an independent measurement of $v \sin i_\star$.
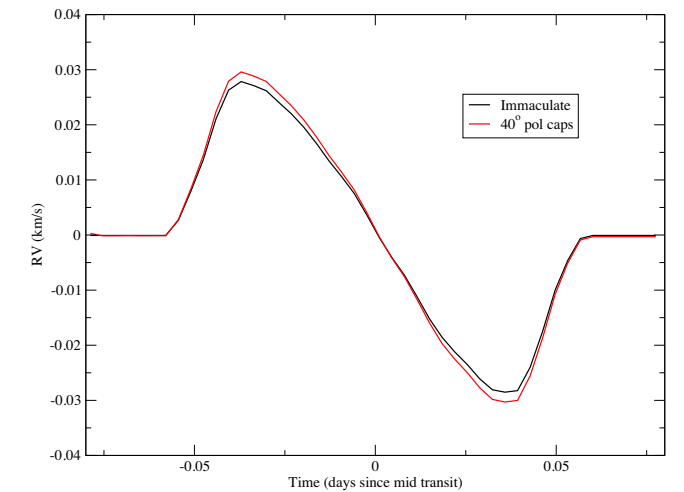
3.2 About the colour of WASP-80b

Flux-drops during occultation can be combined with the apparent magnitudes of WASP-80, as measured by *WISE* (Wright et al. 2010) in its *W*1 and *W*2 channels (equivalent to *Spitzer*'s channels 1 and 2; Triaud et al. 2014) to compute WASP-80b's dayside apparent magnitudes: $m_{[3.6]} = 16.63 \pm 0.26$ and $m_{[4.5]} = 15.872 \pm 0.078$. This implies a very red colour for WASP-80b: $[3.6]-[4.5] = 0.76 \pm 0.27$, compared to the average colour of hot Jupiters of 0.149 ± 0.025 (sample taken from Triaud et al. (2014), except for one significantly updated value on HD 209458b; Zellem et al. 2014).

We reproduced the methodology applied in Triaud et al. (2014) and find that the WASP-80 system has a distance modulus
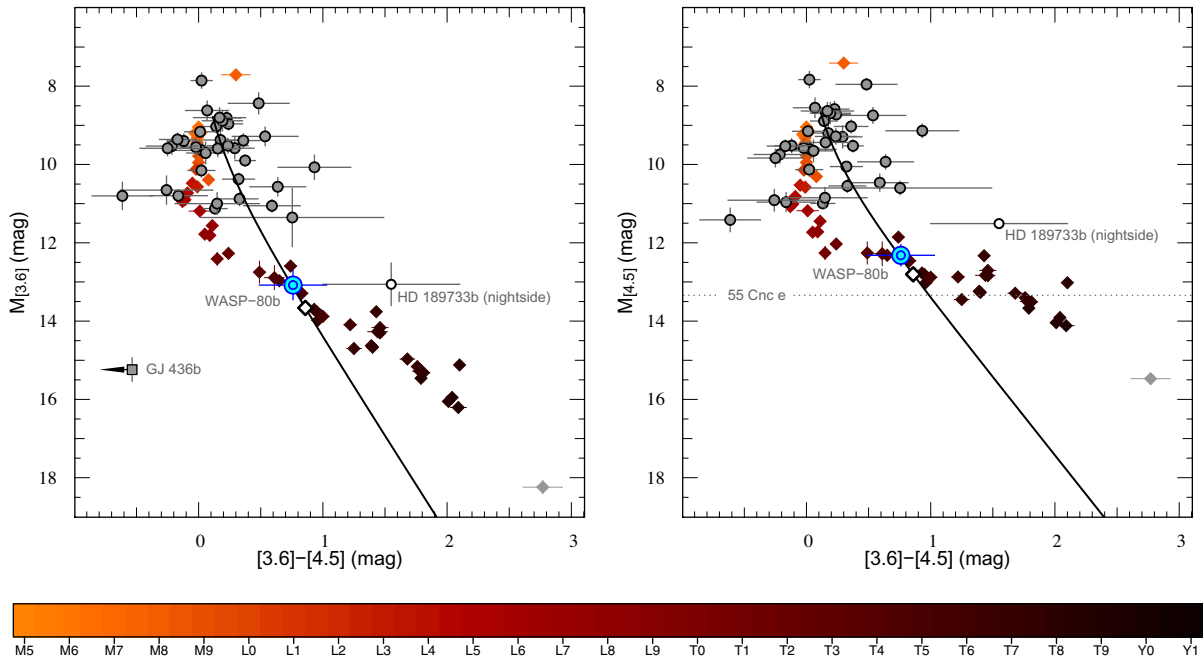
Figure 4. Two colour–magnitude diagrams highlighting the position of the dayside of WASP-80b. Circles represent planets; GJ 436b and the nightside of HD 189733Ab have slightly different symbols to attract attention. Diamonds show the location of ultracool dwarfs obtained from Dupuy & Liu (2012), colour-coded as a function of spectral type. Grey symbols indicate no spectral classification. The blackline outlines the location of blackbodies with of a size similar to WASP-80b, but with effective temperatures ranging from 4000 to 400 K. The empty diamond on this line show 800 K. WASP-80b has one of the reddest dayside amongst all hot Jupiters, but remains bluer than HD 189733Ab's nightside.

$m - M = 3.55 \pm 0.26$ (51.3 $\pm$ 6.2 pc). The absolute magnitudes of WASP-80b's dayside are therefore: $M_{[3.6]} = 13.08 \pm 0.37$ and $M_{[4.5]} = 12.32 \pm 0.27$. This is slightly fainter than the nightside of HD 189733Ab; it is also bluer in those specific bands (Knutson et al. 2012; Triaud 2014).

The *Spitzer* occultations correspond to brightness temperatures of 901^{+68}_{-72} and 888^{+57}_{-58} K for channel 1 and 2, respectively, slightly above its equilibrium temperature of 800 K. These values have been computed using the stellar models, computed by Kurucz (1993), that were compatible with the stellar parameters that we have used for WASP-80. The error budget contains the observational uncertainties on the occultations' depths and on the stellar parameters, as in Demory et al. (2013).

Dupuy & Liu (2012) present relations between absolute magnitudes in certain bandpasses, including those we observed in, and spectral classification of ultracool dwarfs. The dayside of WASP-80b corresponds to a T4 dwarf, in both the [3.6] and [4.5] channels. T4 is the latest type considered within the L–T transition. The T4 type comprises effective temperatures ranging between 1100 and 1300 K (Stephens et al. 2009). A 200 K increase can be compensated by a 30 per cent reduction in radius and produce a similar luminosity. According to Baraffe et al. (2003), brown dwarfs can be 0.75 $R_{\rm Jup}$, which would make WASP-80b's dayside fitted with a T4's flux, within uncertainties. Provided that this is indeed the case, our results may imply that for planets, the L–T transition happens at cooler temperatures than for brown dwarfs.[4]

We do not intend here to attach a spectral classification to WASP-80b, but only to provide a reference point. These relations have been built from – and are therefore only valid for – ultracool dwarfs: self-

luminous objects, whose stronger gravities impact the structure and type of clouds layers. While for brown dwarfs, a change in composition leads to small variations in the emerging spectrum, planetary spectra can be severely affected. This is particularly relevant since planets cover an important range in metal enrichment as seen in the Solar system. For similar composition, irradiation changes a planet's spectrum dramatically too (Burrows 2014) and different chemistry can be expected between the night and daysides of a planet, rendering the classification of a planet arduous at best (Cooper & Showman 2006). Indeed, the phase curve of HD 189733Ab presents evidence that its atmosphere goes through a change in colour similar to a spatial transition between L and T (Triaud 2014).

Our values were placed into two colour–magnitude diagrams (Fig. 4), presenting the same data as in Triaud et al. (2014) (except for HD 209458b; Zellem et al. 2014 and the nightside of HD 189733Ab; Triaud 2014). WASP-80b sits just on the T-dwarf sequence, which confirms our earlier statement about its resemblance to a T4 spectral type. The redward direction of the T-dwarf sequence (in the [3.6]−[4.5] colour) is characterized by the appearance of strengthening CH_4 absorption in the 3.6 µm channel (and a corresponding decrease in CO: see Patten et al. 2006; Zahnle & Marley 2014).

Two blackbody loci, corresponding to a given size of 1 $R_{\rm Jup}$, for all effective temperatures between 4000 and 400 K, are also drawn on Fig. 4, with a mark where 800 K is. WASP-80b coincides with blackbodies of temperatures 890^{+80}_{-60} and 900^{+60}_{-40} K for [3.6] and [4.5 µm], respectively. These temperatures are equivalent to brightness temperatures but are estimated differently than the values provided in Table 1. In this new approach, we make no assumption on the shape of the stellar photosphere, but instead are dependent on the assumed distance. It is reassuring to see agreement between these two different methods.

---

[4] that transition is expected to occur around 500 K (Zahnle & Marley 2014). However, their work was carried for self-luminous objects only.

Table 2. Predicted magnitudes and occultation depth for various broad-bands, and for two scenarios representing the two alternatives for WASP-80b: a T4 spectrum, or a blackbody. To compute the magnitude for the T4 type, we used the relations produced in Dupuy & Liu (2012), with their errors. The uncertainty on the distance is propagated to provide a credible range of values. Our detections fall within those boundaries. Those errors are only useful when considering each band in isolation. Occultations depth were estimated using stellar visual magnitudes obtained from *WISE* (Cutri & et al. 2013) and 2MASS (Skrutskie et al. 2006).

Band	Absolute magnitude	Visual magnitude	Occultation depth [ppm]
	if a T4		
J_{2MASS}	14.3 ± 0.4	17.9 ± 0.5	340 ± 180
H_{2MASS}	14.1 ± 0.4	17.7 ± 0.5	210 ± 120
K_{2MASS}	14.1 ± 0.4	17.7 ± 0.5	182 ± 98
[3.6]	12.9 ± 0.3	16.5 ± 0.4	520 ± 210
[4.5]	12.3 ± 0.2	15.9 ± 0.3	930 ± 270
[5.8]	12.0 ± 0.3	15.6 ± 0.4	1150 ± 470
	if a 900 K blackbody		
J_{2MASS}	20.7	24.3 ± 0.25	1.0 ± 0.2
H_{2MASS}	17.5	21.1 ± 0.25	9.2 ± 2.2
K_{2MASS}	15.5	19.1 ± 0.25	50 ± 12
[3.6]	13.0	16.6 ± 0.25	480 ± 110
[4.5]	12.3	15.9 ± 0.25	930 ± 220
[5.8]	11.7	15.3 ± 0.26	1510 ± 370

In the [3.6]−[4.5] colour, the T-dwarf sequence and the blackbody both slope towards redder colours. This is in contrast to the near-IR *J*, *H*, *K*s and mid-IR [5.8 μm] bands where the L–T transition is characterized by a blueward slope (while the blackbody

remains redward; Triaud et al. 2014). Predictions are presented in Table 2. Observing in the *J*, *H* and *K*s bands is particularly promising to distinguish between both propositions.

The brown dwarf sequences and the blackbody expectations are furthest apart, over the two *Warm Spitzer* channels, for planets with equilibrium temperatures intermediate between WASP-80b and 1000 K (e.g. WASP-8b; Cubillos et al. 2013). Observations of additional systems in this range will help interpret the results for WASP-80b. Those observations would also verify the existence of diversifying atmospheric properties with increasing magnitude, as revealed by an increase in the range of colour occupied by cooler planets (Triaud et al. 2014).

3.3 About the transmission spectrum

The planet-star radius ratio ($R_p/R_\star$) in each of our broad bandpasses can be found at the bottom of Table 1. They are graphically presented in Fig. 5, and except for the value at 0.47 μm, are all consistent with each other. The inverse-variance weighted average of these values is $R_p/R_\star = 0.171\,67 \pm 0.000\,20$, which is also plotted on Fig. 5. The data agree well with a horizontal line: $\chi^2 = 8.3 \pm 4.1$, which for 6 degrees of freedom (seven wavelengths and one free parameter) makes a reduced $\chi_r^2 = 1.4 \pm 0.7$. We see no reason to compare our data to more complex models (even a slope would be too much). Our analysis refines the results of Mancini et al. (2014). WASP-80b joins a number of hot Jupiters whose spectra are approximately flat within measurement errors (e.g. Mancini et al. 2013; Pont et al. 2013). Flat transmission spectra have also been observed for warm Neptunes such as GJ 1214b (Berta et al. 2012; Kreidberg et al. 2014), GJ 436b (Knutson et al. 2014), GJ 3470b (Ehrenreich et al. 2014), a result that has been interpreted as indicating the presence of clouds or as a sign of high metal content.
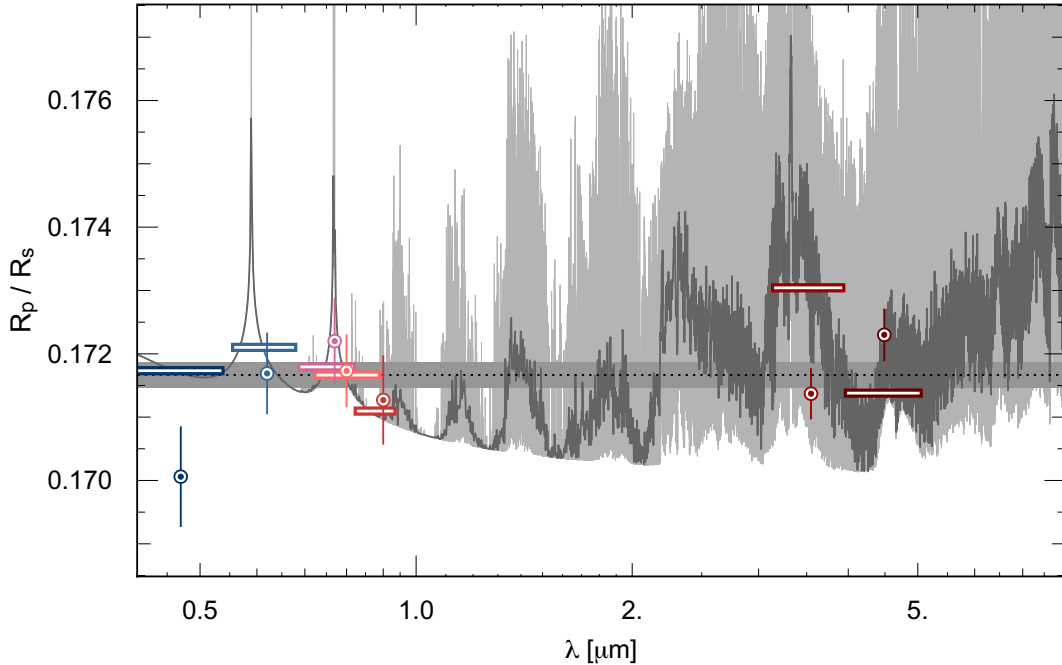

Figure 5. Ratios of the planet to star radii as a function of wavelength. The dotted line is the weighed mean, and the grey area the error on that mean. A model atmosphere (H$_2$: 93 per cent, He: 7 per cent, H$_2$O: 10^{-4}, CH$_4$: 10^{-4}, CO: 10^{-4}, Na: 10^{-6} and K: 10^{-7}) is also displayed, with two different resolutions, drawn using different shades. This model is not fitted, and is here purely for illustrative purposes. Coloured bars correspond to the measurements as expected from the model; their widths illustrate the full width at half-maximum of their respective filters.

Fukui et al. (2014) also observed WASP-80b. They find $R_p/R_\star = 0.170\,00 \pm 0.000\,40$ (averaged over the *J*, *H* and *K*$_s$ bands, who are all consistent with each other) a value similar to the measurement at 0.45 μm (Sloan g') shown in Fig. 5. In the visible they measure $R_p/R_\star = 0.1741 \pm 0.0010$, which is higher than what we find.[5] In their analysis, some transit parameters were kept fixed which usually results in underestimated error bars and would make any dispersion appear statistically more significant than it really is. For this reason, we have not included their results in our analysis.

If the redness of WASP-80b's dayside is an indication of methane absorption, then a corresponding signature is to be expected in transmission. Fortney et al. (2010) present models for planets with equilibrium temperatures of 1000 and 500 K. While the former remains mostly influenced by H_2O, Na and K absorption, the latter shows a transition to an atmosphere dominated by CH_4 absorption, closer to what we expect in the case of WASP-80b. This simple picture can be considerably altered in the presence of an opaque cloud cover (possibly assembled from soots, created through via photochemical reactions with methane; Moses et al. 2011).

For illustrative purposes, we calculated a model spectrum for WASP-80b, which we display in Fig. 5 (Ehrenreich et al. 2006, 2014).[6] It was set with the following abundances: H_2: 93 per cent, He: 7 per cent, H_2O: 10^{-4}, CH_4: 10^{-4}, CO: 10^{-4}, Na: 10^{-6} and K: 10^{-7} as in Moses et al. (2011). The visible regions are dominated by alkali absorption, with some Rayleigh scattering, produced purely from H_2. We note that the bluest measurement is particularly discrepant to that model. A visual comparison of that model to our data also shows that one of the strongest methane features peaks around 3.5 μm. Methane should enhance a planet's radius at [3.6] compared to [4.5], which we do not see in transmission (although we detect an equivalent effect in emission). This is the most we can reliably affirm.

4 CONCLUSION

WASP-80b is on an aligned orbit and is the second faintest planet with an emission measured in each of the *Warm Spitzer* channels, after GJ 436b at [3.6] (Lanotte et al. 2014) and 55 Cnc e at [4.5] (Demory et al. 2012), which are indicated in Fig. 4. It is the faintest measured in both bands and for which a colour can be computed. The planet's dayside is amongst the three reddest daysides of any hot Jupiter. HD 189733Ab's nightside remains the measurement furthest to the red (Knutson et al. 2012; Triaud 2014).

GJ 436b and WASP-80b have similar equilibrium temperatures (Stevenson et al. 2010) and both show a flat spectrum (Knutson et al. 2014). However, we find that their colours are radically different which can be interpreted as evidence for different chemical compositions (as proposed in Stevenson et al. 2010 and Lanotte et al. 2014). We note here that GJ 436b has a radius significantly smaller than WASP-80b's; one could wonder if both ought to be compared since gravity has an important role to play on the condensation of chemical species into clouds layers (GJ 436b is 2.3 times denser than WASP-80b). However, we find that there is some credence to that: a change in radius will cause a change in absolute magnitude. Correcting GJ 436b's radius to WASP-80b's (1 R_{Jup}) amounts to comparing absolute magnitude produced by similar areas. If it were that large, GJ 436b would be 2.1 mag brighter. Using the values pre-

sented in Triaud et al. (2014), this would mean an $M_{[3.6]} = 13.13 \pm 0.28$, on a par with WASP-80b. Both planets emit a similar flux density at 3.6 μm (while remaining very different at 4.5 μm).

WASP-80b's atmosphere is ambiguous. While WASP-80b presents a dayside with a luminosity and a colour reminiscent of a mid-T dwarf (who have a patchy cloud cover and methane absorption), its transmission spectrum appears featureless (implying overcast, without direct evidence for methane). The planet is also entirely compatible with a blackbody. Upfront the current data would fit well with WASP-80b being a dusty isothermally radiating ball. However, some brown dwarfs too are compatible with blackbody colours and would too present a flat transmission. Instead, direct spectroscopy shows they are far from resembling blackbodies. We need to keep entertaining the possibility that neither is WASP-80b.

Is WASP-80b a T4? Likely not. If we have learned anything about exoplanets, is that they beat our simplest explanations. However, its current position in the colour–magnitude diagram permits us to raise interesting questions. These diagrams become a reading grid. More observations are dearly needed to first, verify WASP-80b's colour, especially in the 3.6 μm band where our detection is only at the 4σ level and secondly, to scrutinize the planet's size as a function of wavelength in the near-infrared, in search for some weak methane absorption. Alternatively, occultation measurements in the near-infrared would confirm whether the planet obeys a T dwarf behaviour, constraint its flux to a blackbody, or uncover its own planetary behaviour.

The methods developed by Snellen et al. (2010) to detect CO and H_2O in absorption and in emission in exoplanets (e.g. Rodler, Lopez-Morales & Ribas 2012; Birkby et al. 2013) could in principle be used to probe for the presence of methane. Observations have been attempted at the VLT using CRIRES targeting a region containing a forest of CH_4 lines, around 2.3 μm. However, bad weather and scheduling issues meant that fewer transits were obtained than requested. CRIRES has now been unmounted from the telescope for upgrade.

Would a transmission spectrum turn out to show no spectral signatures, we could postulate the following:

(i) WASP-80b is a featureless blackbody, presumably because of a dusty/cloudy atmosphere, that just happened to coincide with the T-dwarf sequence.

(ii) WASP-80b is part of a diverse population of *warm* planets enveloped by a greater variety of atmospheres than brown dwarfs have, as proposed in Triaud et al. (2014). WASP-80b's position at the conjunction between blackbody and T-dwarfs would therefore be a coincidence. If indeed the case, it implies that its composition cannot be inferred from comparing with ultracool dwarfs, such as T-dwarfs, whose atmospheric chemistry and optical properties would share little in common with planets (e.g. Zahnle & Marley 2014), especially the irradiated kind.

(iii) WASP-80b's colour is an integrated view of its dayside surface which may be inhomogeneous (such as Kepler-7b; Demory et al. 2013). The hottest parts are possibly covered in clouds (such as L dwarfs and early-type T-dwarfs), while the colder zones of the dayside may remain free, clouds having rained out. Equatorial wind could move enough of the clouds to the night side, traversing the terminator and affecting the resulting transmitted spectrum.

To complicate further, the range of colour indices covered by the colder gas giants may be produced by clouds covers having distinct optical properties, for instance, if trace elements specific to some planet react with the surfaces of suspended cloud particles, leading to different albedos and opacities. In addition, extra diversity can

---

[5] those values only account for their transit depths, after removing those of Mancini et al. (2014) which they had included too.
[6] nota bene: this model does not solve to radiative equilibrium.

be caused by planets possessing a different number and alternation of *belts* and *zones* with contrasting albedos (Jupiter and Saturn are dissimilar).

Most of these considerations rely on the fact that brown dwarfs and planets can be compared to each other directly. The exercise is currently useful since the brown dwarfs are well understood and that the planets are not. Eventually, we will come to study each population in isolation once planetary-specific behaviour has been identified. Reasons range from the irradiated conditions of hot Jupiters, to being in a different gravity range compared to brown dwarfs. Chemical transitions very likely differ between brown dwarfs and planets. Gravity influences the chemical balance between CO and CH_4 (Zahnle & Marley 2014). This would blunt the sharp L–T transition and cause a shallower slope in the $[3.6]-[4.5]$ colour than for brown dwarfs, making it closer to a blackbody.

Currently, it remains unclear whether WASP-80b's atmosphere contains any methane. Few planets have been observed near the L/T transition. Apart from WASP-80b, most are young, directly imaged systems which despite distinctive physical parameters, present similar atmospheric characteristics: they are close to blackbodies (in near-IR; Triaud et al. (2014)), likely cloudy (Marley et al. 2012), and offer methane absorption lower than expected (Konopacky et al. 2013). As such, deepening the study of WASP-80b will prove important. Parallel properties between the massive, far flung giants orbiting a young A star, and the light, mildly irradiated giant orbiting an M dwarf would inform us about widely occurring phenomena in exoplanets (be they related to atmospheric physics or to formation processes).

Doubtless to say, other systems intermediate between the general population of hot Jupiters and WASP-80b would be fascinating to observe, in order to study where they land in colour–magnitude diagrams. Observing the shape of their transmitted spectra can bring to the fore a relation between colour and chemical composition/clouds presence.

NOTA BENE

Dates are given in the BJD-UTC standard. The radii we used for Jupiter and the Sun are the volumetric mean radii.

ACKNOWLEDGEMENTS

REFERENCES

Ackerman A. S., Marley M. S., 2001, ApJ, 556, 872
Albrecht S. et al., 2011, ApJ, 738, 50
Artigau É., Bouchard S., Doyon R., Lafrenière D., 2009, ApJ, 701, 1534
Baraffe I., Chabrier G., Barman T. S., Allard F., Hauschildt P. H., 2003, A&A, 402, 701
Berta Z. K. et al., 2012, ApJ, 747, 35
Birkby J. L., de Kok R. J., Brogi M., de Mooij E. J. W., Schwarz H., Albrecht S., Snellen I. A. G., 2013, MNRAS, 436, L35
Bolton S. J., the Juno Science Team, 2010, in Barbieri C., Chakrabarti S., Coradini M., Lazzarin M., eds, Proc. IAU Symp. 269, Galileo's Medicean Moons: Their Impact on 400 Years of Discovery. Cambridge Univ. Press, Cambridge, p. 92
Buenzli E., Apai D., Radigan J., Reid I. N., Flateau D., 2014, ApJ, 782, 77
Burgasser A. J., Marley M. S., Ackerman A. S., Saumon D., Lodders K., Dahn C. C., Harris H. C., Kirkpatrick J. D., 2002, ApJ, 571, L151
Burrows A. S., 2014, Proc. Natl. Acad. Sci., 111, 12601
Claret A., Bloemen S., 2011, A&A, 529, A75
Collier Cameron A. et al., 2007, MNRAS, 375, 951
Cooper C. S., Showman A. P., 2006, ApJ, 649, 1048
Crossfield I. J. M. et al., 2014, Nature, 505, 654
Cubillos P. et al., 2013, ApJ, 768, 42
Cutri R. M. et al., 2013, VizieR Online Data Catalog, 2328, 0
Demory B.-O., Seager S., 2011, ApJS, 197, 12
Demory B.-O., Gillon M., Seager S., Benneke B., Deming D., Jackson B., 2012, ApJ, 751, L28
Demory B.-O. et al., 2013, ApJ, 776, L25
Doyle A. P., Davies G. R., Smalley B., Chaplin W. J., Elsworth Y., 2014, MNRAS, 444, 3592
Dupuy T. J., Liu M. C., 2012, ApJS, 201, 19
Ehrenreich D., Tinetti G., Lecavelier Des Etangs A., Vidal-Madjar A., Selsis F., 2006, A&A, 448, 379
Ehrenreich D. et al., 2014, A&A, 570, A89
Fazio G. G. et al., 2004, ApJS, 154, 10
Fortney J. J., Shabram M., Showman A. P., Lian Y., Freedman R. S., Marley M. S., Lewis N. K., 2010, ApJ, 709, 1396
Fraine J. et al., 2014, Nature, 513, 526
Fukui A. et al., 2014, ApJ, 790, 108
Gelman A., Rubin D. B., 1992, Stat. Sci., 7, 457
Gillon M. et al., 2012, A&A, 542, A4
Gillon M., Triaud A. H. M. J., Jehin E., Delrez L., Opitom C., Magain P., Lendl M., Queloz D., 2013, A&A, 555, L5
Gillon M. et al., 2014, A&A, 563, A21
Giménez A., 2006, ApJ, 650, 408
Gray D. F., 2008, in Gray D. F., ed., The Observation and Analysis of Stellar Photospheres. Cambridge Univ. Press, Cambridge
Hellier C. et al., 2012, MNRAS, 426, 739

Herrero E., Ribas I., Jordi C., 2014, Exp. Astron., available at: http://link.springer.com/article/10.1007%2Fs10686-014-9387-0

Jehin E. et al., 2011, The Messenger, 145, 2

Jordán A. et al., 2013, ApJ, 778, 184

Kirkpatrick J. D., 2005, ARA&A, 43, 195

Knutson H. A., Charbonneau D., Allen L. E., Burrows A., Megeath S. T., 2008, ApJ, 673, 526

Knutson H. A. et al., 2012, ApJ, 754, 22

Knutson H. A., Benneke B., Deming D., Homeier D., 2014, Nature, 505, 66

Konopacky Q. M., Barman T. S., Macintosh B. A., Marois C., 2013, Science, 339, 1398

Kreidberg L. et al., 2014, Nature, 505, 69

Kurucz R., 1993, Kurucz CD-ROM No. 13. ATLAS9 Stellar Atmosphere Programs and 2 km/s grid. Smithsonian Astrophysical Observatory, Cambridge, MA

Lanotte A. A. et al., 2014, A&A, 572, A73

Lewis N. K. et al., 2013, ApJ, 766, 95

Lin D. N. C., Bodenheimer P., Richardson D. C., 1996, Nature, 380, 606

López-Morales M. et al., 2014, ApJ, 792, L31

McCullough P. R., Crouzet N., Deming D., Madhusudhan N., 2014, ApJ, 791, 55

Madhusudhan N., Crouzet N., McCullough P. R., Deming D., Hedges C., 2014, ApJ, 791, L9

Mancini L. et al., 2013, MNRAS, 430, 2932

Mancini L. et al., 2014, A&A, 562, A126

Mandel K., Agol E., 2002, ApJ, 580, L171

Mandell A. M., Haynes K., Sinukoff E., Madhusudhan N., Burrows A., Deming D., 2013, ApJ, 779, 128

Marley M. S., Saumon D., Cushing M., Ackerman A. S., Fortney J. J., Freedman R., 2012, ApJ, 754, 135

Mayor M., Queloz D., 1995, Nature, 378, 355

Moses J. I. et al., 2011, ApJ, 737, 15

Öberg K. I., Murray-Clay R., Bergin E. A., 2011, ApJ, 743, L16

Patten B. M. et al., 2006, ApJ, 651, 502

Pollacco D. L. et al., 2006, PASP, 118, 1407

Pont F., Sing D. K., Gibson N. P., Aigrain S., Henry G., Husnoo N., 2013, MNRAS, 432, 2917

Radigan J., Jayawardhana R., Lafrenière D., Artigau É., Marley M., Saumon D., 2012, ApJ, 750, 105

Rasio F. A., Ford E. B., 1996, Science, 274, 954

Rodler F., Lopez-Morales M., Ribas I., 2012, ApJ, 753, L25

Schlaufman K. C., 2010, ApJ, 719, 602

Schneider J., Dedieu C., Le Sidaner P., Savalle R., Zolotukhin I., 2011, A&A, 532, A79

Schwarz G., 1978, Ann. Stat., 6, 461

Seager S., Deming D., 2010, ARA&A, 48, 631

Sing D. K. et al., 2011, MNRAS, 416, 1443

Skrutskie M. F. et al., 2006, AJ, 131, 1163

Snellen I. A. G., de Kok R. J., de Mooij E. J. W., Albrecht S., 2010, Nature, 465, 1049

Stephens D. C. et al., 2009, ApJ, 702, 154

Stetson P. B., 1987, PASP, 99, 191

Stevenson K. B. et al., 2010, Nature, 464, 1161

Stevenson K. B. et al., 2012, ApJ, 754, 136

Triaud A. H. M. J., 2014, MNRAS, 439, L61

Triaud A. H. M. J. et al., 2011, A&A, 531, A24

Triaud A. H. M. J. et al., 2013, A&A, 551, A80

Triaud A. H. M. J., Lanotte A. A., Smalley B., Gillon M., 2014, MNRAS, 444, 711

Winn J. N., Fabrycky D., Albrecht S., Johnson J. A., 2010, ApJ, 718, L145

Wright E. L. et al., 2010, AJ, 140, 1868

Wright J. T. et al., 2011, PASP, 123, 412

Zahnle K. J., Marley M. S., 2014, ApJ, 797, 41

Zellem R. T. et al., 2014, ApJ, 790, 53

APPENDIX A:

Here are located the graphical representation of each photometric time series that has been used in our analysis, including the corrections given to the data. Table A1 contains the journal of observations and type of corrections applied to the data.

Table A1. WASP-80 b photometric eclipse time series used in this work. For each light curve, this table shows the date of acquisition, the used instrument and filter, the exposure time $T_{\rm exp}$, the number of data points, the baseline function selected for our global analysis (see Section 2.3), the error correction factor CF used in our global analysis, and the nature of the eclipse (transit or occultation). For the baseline function, $p(\epsilon^N)$ denotes, respectively, an N-order polynomial function of time ($\epsilon = t$), the logarithm of time ($\epsilon = l$), x and y positions ($\epsilon = xy$), full width at half-maximum FWHM ($\epsilon = {\rm fwhm}$) and FWHM in the x-direction ($\epsilon = {\rm fwhm}_x$); o denotes an offset at the time of a meridian flip of TRAPPIST (see Gillon et al. 2012); BM denotes the use of the BLISS-mapping technique (Stevenson et al. 2012) to improve the modelling of the position effects (see Gillon et al. 2014).

| Date	Instrument	Instrument	Filter	$T_{\rm exp}$	N_p	Baseline function	CF	Eclipse type
7 May 2012	TRAPPIST	TRAPPIST	Sloan z'	10 s	728	$p(t^2) + o$	2.08	Transit
26 Jul 2012	*Euler*	*Euler*	Gunn r'	60 s	208	$p(t^2 + {\rm fwhm}^2)$	1.36	Transit
10 Sep 2012	TRAPPIST	TRAPPIST	Sloan z'	10 s	705	$p(t^2)$	1.15	Transit
13 Jun 2013	TRAPPIST	TRAPPIST	Sloan z'	13 s	749	$p(t^2) + o$	1.20	Transit
16 Jun 2013	TRAPPIST	TRAPPIST	Sloan z'	13 s	782	$p(t^2 + xy^2) + o$	1.49	Transit
16 Jun 2013	*Euler*	*Euler*	Gunn r'	50 s	175	$p(t^2)$	2.86	Transit
16 Jun 2013	2.2m/GROND	2.2m/GROND	Sloan z'	60 s	157	$p(t^2)$	2.64	Transit
16 Jun 2013	*Danish*/DFOSC	*Danish*/DFOSC	Bessell I	60 s	200	$p(t^2)$	1.05	Transit
16 Jun 2013	2.2m/GROND	2.2m/GROND	Sloan r'	60 s	156	$p(t^2)$	2.14	Transit
16 Jun 2013	2.2m/GROND	2.2m/GROND	Sloan i'	60 s	156	$p(t^2)$	1.05	Transit
16 Jun 2013	2.2m/GROND	2.2m/GROND	Sloan g'	60 s	162	$p(t^2)$	0.76	Transit
3 Jul 2013	*Spitzer*	*Spitzer*	3.6 μm		548	$p(xy^2 + l^1) + {\rm BM}$	1.35	occultation
13 Jul 2013	*Spitzer*	*Spitzer*	4.5 μm		123	$p({\rm fwhm}_x^1 + xy^2 + l^1)$	1.06	Transit
18 Jul 2013	*Spitzer*	*Spitzer*	4.5 μm		121	$p(xy^2 + l^1)$	0.68	occultation
24 Jul 2013	*Spitzer*	*Spitzer*	3.6 μm		569	$p({\rm fwhm}_x^1 + xy^2 + l^1) + {\rm BM}$	1.78	occultation
27 Jul 2013	*Spitzer*	*Spitzer*	4.5 μm		123	$p({\rm fwhm}_x^1 + xy^2 + l^1)$	1.14	occultation
1 Aug 2013	*Spitzer*	*Spitzer*	3.6 μm		579	$p({\rm fwhm}_x^1 + xy^2 + l^1) + {\rm BM}$	1.33	Transit
1 Aug 2013	TRAPPIST	TRAPPIST	Sloan z'	13s	512	$p(t^2)$	1.23	Transit
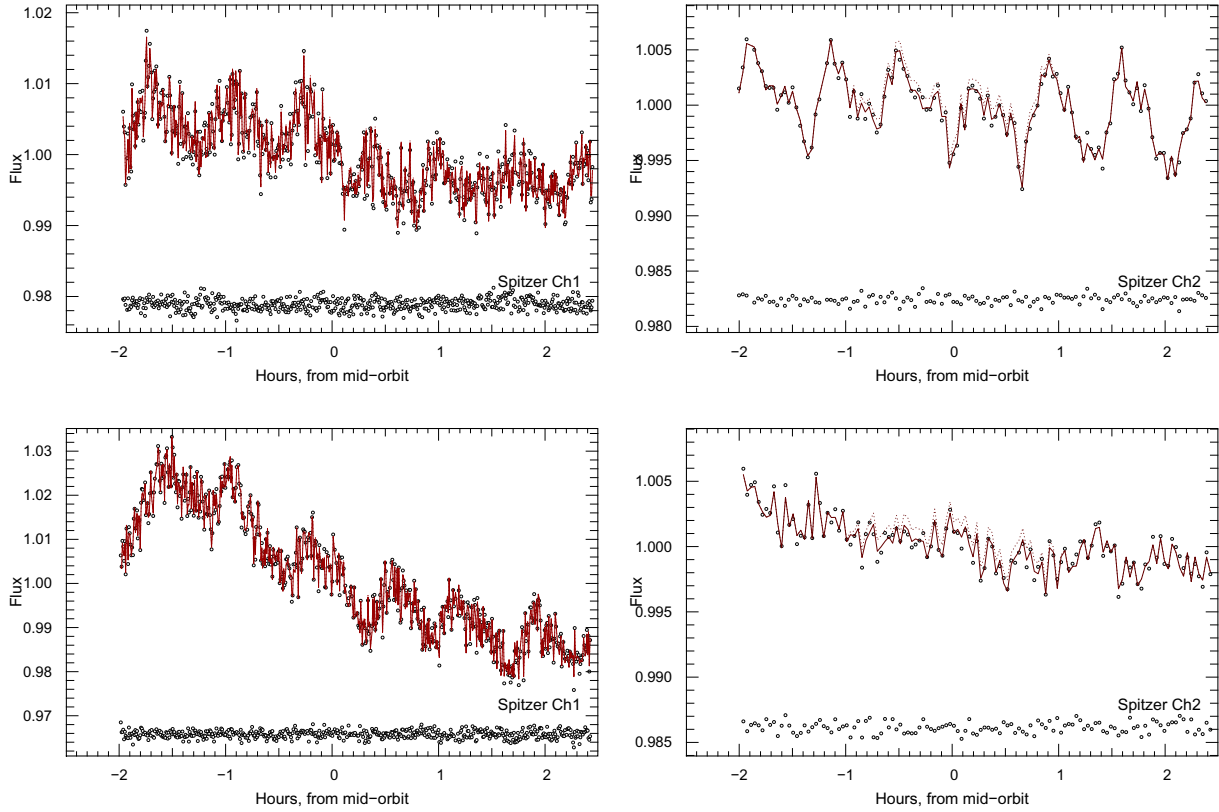
Figure A1. Photometry at occultation, as extracted from the *Warm Spitzer* frames, in both channels, with the initial ramp removed. The full model to the data is shown as a plain line; the residuals are displayed underneath. The corrections, including the variations in intrapixel sensitivity, are isolated and drawn as a dotted line (barely noticeable here due to the weakness of the occupation signal compared to the corrections).
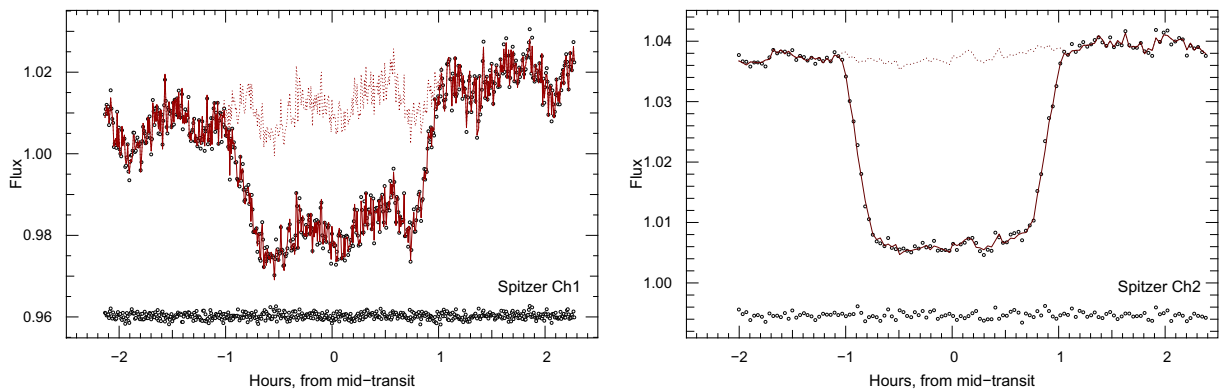

Figure A2. Photometry at transit, as extracted from the *Warm Spitzer* frames, in both channels, with the initial ramp removed. The full model to the data is shown as a plain line; the residuals are displayed underneath. The corrections, including the variations in intrapixel sensitivity, are isolated and drawn as a dotted line.
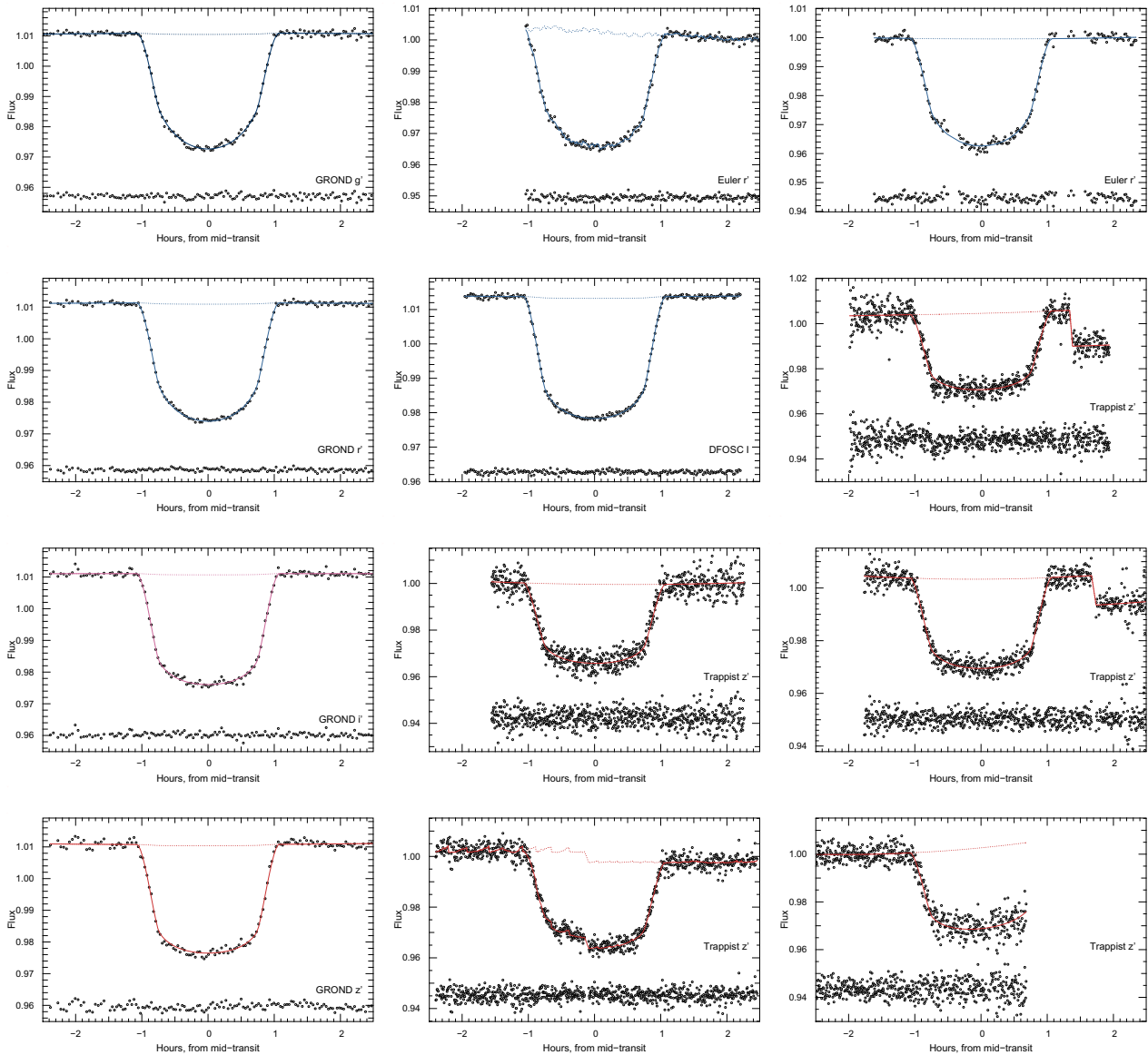
Figure A3. Photometry at transit, in the visible wavelengths. The full model to the data is shown as a plain line; the residuals are displayed underneath. The corrections, for instance airmass, or changes in seeing or pointing, are isolated and drawn as a dotted line.

SUPPORTING INFORMATION

Additional Supporting Information may be found in the online version of this article:

(http://mnras.oxfordjournals.org/lookup/suppl/doi:10.1093/mnras/stv706/-/DC1).

Please note: Oxford University Press are not responsible for the content or functionality of any supporting materials supplied by the authors. Any queries (other than missing material) should be directed to the corresponding author for the paper.

[1] *Centre for Planetary Sciences, University of Toronto at Scarborough, 1265 Military Trail, Toronto, ON M1C 1A4, Canada*
[2] *Department of Astronomy & Astrophysics, University of Toronto, Toronto, ON M5S 3H4, Canada*
[3] *Kavli Institute for Astrophysics & Space Research, Massachusetts Institute of Technology, Cambridge, MA 02139, USA*

[4] *Institut d'Astrophysique et de Géophysique, Université de Liège, Allée du 6 Août 17, Sart Tilman, B-4000 Liège 1, Belgium*
[5] *Observatoire Astronomique de l'Université de Genève, Chemin des Maillettes 51, CH-1290 Sauverny, Switzerland*
[6] *Institut de Ciències de l'Espai (CSIC-IEEC), Campus UAB, Facultat de Ciències, Torre C5 parell, 2a pl, E-08193 Bellaterra, Spain*
[7] *Astrophysics Group, Keele University, Staffordshire ST5 5BG, UK*
[8] *SUPA, School of Physics & Astronomy, University of St Andrews, North Haugh, St Andrews, Fife KY16 9SS, UK*
[9] *Cavendish Laboratory, J J Thomson Avenue, Cambridge CB3 0HE, UK*
[10] *Center for Space and Habitability, University of Bern, Sidlerstrasse 5, CH-3012 Bern, Switzerland*
[11] *Department of Physics, University of Warwick, Coventry CV4 7AL, UK*
[12] *N. Copernicus Astronomical Centre, Polish Academy of Sciences, Bartycka 18, PL-00-716 Warsaw, Poland*

This paper has been typeset from a TEX/LATEX file prepared by the author.